Computer-Aided Design 164 (2023) 103589

Contents lists available at ScienceDirect

Computer-Aided Design

journal homepage: www.elsevier.com/locate/cad

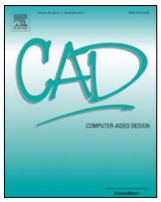

Subdivision-based IGA Coupled EIEQ Method for the Cahn–Hilliard Phase-Field Model of Homopolymer Blends on Complex Surfaces

Qing Pan [a], Chong Chen [b], Timon Rabczuk [c], Jin Zhang [a], Xiaofeng Yang [d,*]

[a] School of Computer and Communication Engineering, Changsha University of Science & Technology, Changsha, 410114, China
[b] LSEC, ICMSEC, Academy of Mathematics and Systems Science, Chinese Academy of Sciences, Beijing, 100190, China
[c] Institute of Structural Mechanics, Bauhaus Universität-Weimar, Weimar, 99423, Germany
[d] Department of Mathematics, University of South Carolina, Columbia, SC 29208, USA

ARTICLE INFO

Article history:
Received 25 February 2023
Received in revised form 13 June 2023
Accepted 1 July 2023

Keywords:
Loop subdivision
IGA-EIEQ
Decoupled
Unconditional energy stability
Phase-field model
Homopolymer blends

ABSTRACT

In this paper, we construct an IGA-EIEQ coupling scheme to solve the phase-field model of homopolymer blends on complex subdivision surfaces, in which the total free energy contains a gradient entropy with a concentration-dependent de-Gennes type coefficient and a non-linear logarithmic Flory–Huggins type potential. Based on the EIEQ method, we develop a fully-discrete numerical scheme with the superior properties of linearity, unconditional energy stability, and second-order time accuracy. All we need to do with this fourth-order system is to solve some constant-coefficient elliptic equations by applying a new nonlocal splitting techniqueWe then provide detailed proof of the unconditional energy stability and the practical implementation process. Subdivision approaches show a robust and elegant description of the models with arbitrary topology. Subdivision basis functions serve to define the geometry of the models and represent the numerical solutions. Subdivision-based IGA approach provides us with a good candidate for solving the phase-field model on complex surfaces. We successfully demonstrate the unity of employing subdivision basis functions to describe the geometry and simulate the dynamical behaviors of the phase-field models on surfaces with arbitrary topology. This coupling strategy combining the subdivision-based IGA method and the EIEQ method could be extended to a lot of gradient flow models with complex nonlinearities on complex surfaces.

1. Introduction

It is well known that the Cahn–Hilliard model [1,2] is one of the classical equations of the phase-field models, which was introduced by Cahn and Hilliard in [3]. They are used to describe the coarsening phenomena in a solid and some complicated phase separation. Nowadays, the Cahn–Hilliard equations have been widely applied in many complicated moving interface problems in the area of materials science and fluid dynamics through a phase-field approach. The total free energy of the classical Cahn–Hilliard system consists of the Ginzburg–Landau double well potential and the gradient entropy with the constant coefficient. In this work, we consider numerical approximations of the phase-field model for homopolymer blends [4–7], which could also be called the Stochastic-Cahn–Hilliard equation, or the Cahn–Hilliard–Cook model, since it can be regarded as the Cahn–Hilliard system attached with an external thermal noise named as the stochastic term or the cook-noise [7]. The background of the model dates back decades to the classical modeling work in [4,6,8,9], and has been widely used to simulate the phase transition processes of a blend of two polymer species, or polymer microsphere composite (MMC) hydrogels [10]. The governing equation of the model of homopolymer blends is derived from the energy variation of the total free energy in H^{-1} Sobolev space, whose total free energy includes a logarithmic Flory–Huggins type potential and a gradient entropy with a concentration-dependent de-Gennes type coefficient [6].

There are many successful numerical algorithms for solving partial differential equations (PDEs) on surfaces, where we can refer to the finite difference method in [11], the Spectral method in [12,13], and the finite element method (FEM) in [14], etc. The first two approaches have made significant progress in recent years, however, most of the interest domains are still confined to simple domains, such as circular, rectangular, and spherical regions. Compared with them, the FEM can more effectively deal with a large number of irregular surfaces in the practical engineering, see [15–17] for theoretical/numerical studies of phase transition-related models on surfaces. However, it is remarkable that the FEM involves the approximation of surface differential geometric operators, which may introduce additional errors

* Corresponding author.
E-mail addresses: panqing@lsec.cc.ac.cn (Q. Pan), chench@lsec.cc.ac.cn (C. Chen), timon.rabczuk@uni-weimar.de (T. Rabczuk), jzhang@csust.edu.cn (J. Zhang), xfyang@math.sc.edu (X. Yang).

https://doi.org/10.1016/j.cad.2023.103589
0010-4485/

caused by numerical approximation schemes. Taking the Laplacian operator on a surface as an example, the derivative of the surface itself needs to be integrated. Traditional FEM requires the manual intervention in mesh generation from CAD models, which is costly, time-consuming and labor-intensive, and the refining process is troublesome, especially for the surfaces with complex geometries. Instead of using these methods for solving surface PDE models, this paper adopts the recently developed isogeometric analysis (IGA) framework, see [18,19].

The concept of IGA was proposed to develop a seamless integration between FEM and computer-aided design (CAD), which adopts the non-uniform Rational B-Splines (NURBS) [20–22] or T-splines [23,24] as the same shape functions to describe the solution region and conduct the numerical simulation of PDEs. The framework of IGA is proposed to develop the seamless integration between FEM and computer-aided design (CAD) [25–29]. It has higher numerical accuracy than the FEM, where we can easily implement the *p*-refinement, *h*-refinement, and even *k*-refinement by the technique of the order elevation and the knot insertion. It can remove the interactive communication with the CAD system, then improve the accuracy of the numerical simulation without destroying the original geometric properties. A hybrid phase-field approach in the framework of IGA was developed in [30], which was used to model the crack propagation of functionally graded materials with porosity effects and significantly reduced the computational cost of the phase-field model. In this work, we adopt the efficient subdivision-based IGA approach for solving the phase-field model for homopolymer blends on surfaces. Subdivision is a good candidate in the application of IGA, which has the capability of the refineability of B-spline techniques. Surface subdivision adopts a set of simple and efficient refinement schemes [31–33] to construct smooth surfaces based on arbitrary topological meshes, which can not only conveniently handle complicated geometric forms but also maintain original characteristics near boundaries with angles and creases through straightforward extensions. Both Loop subdivision [34–37] and Catmull–Clark subdivision [38–40] has been developed in IGA. Local refinement and convergence rate [41] was investigated in Catmull–Clark subdivision-based IGA. The optimal convergence rates of hybrid nonuniform subdivision (HNUS) surfaces in IGA was achieved in [42]. Through these research work, we can see that the subdivision-based IGA approach can be viewed as the natural choice for higher-order FEM in engineering practice, see [36,37,43,44] as well.

As for the classical Cahn–Hilliard system, there exist three prevalent numerical techniques of treating the nonlinear term while keeping the energy stability property. The first method is the convex splitting scheme [45], in which we treat the concave term by the explicit form, and treat the convex term of the potential functional by the implicit form. Although the convex splitting method owns the property of energy stability, it introduces nonlinear forms in a lot of cases, so the program implementation is complex and leads to high computational expenditure. The second alternative is the stabilization scheme [46–48], in which we still treat the nonlinear term of the potential functional implicitly, in addition, we consider designing some linear stabilizing terms. We can easily realize these linear schemes, however, one of its shortcomings is that the second-order form only maintains the conditional energy stability [47], that is, the time step size is limited by the thickness of the interface, and the amplitude is small. We want to highlight the third technique called the Invariant Energy Quadratization (IEQ) method [49], where we can treat all nonlinear terms semi-explicitly. The key point of the IEQ method is to change the PDEs resulting from the energy function into an equivalent form including some new variables, then we can treat the nonlinear terms semi-explicitly. Moreover, its first-order and second-order discrete schemes own unconditional energy stability. However, the IEQ method still has some disadvantages, especially in practical implementation. It will result in a linear system with variable coefficients at each time step, see [49–52], therefore to solve a system with variable coefficients, we not only need more complicated computational steps, such as requiring a suitable and robust iterative solver or designing some preconditioner, but also spend more computational time than a linear system with only constant coefficients.

This paper focuses on developing an efficient fully-discrete numerical scheme to solve the phase-field model of homopolymer blends on complex surfaces. In our previous work [53], we introduced a novel framework called IGA-EIEQ time-space-coupling scheme to solve the classical Allen–Cahn and Cahn–Hilliard phase-field models on complex surfaces. However, the phase-field model of homopolymer blends studied in this article is considerably more complex and exhibits distinct nonlinear complexities compared to the classical Cahn–Hilliard equation. In particular, the model under investigation incorporates a logarithmic type bulk potential and a gradient entropy with a non-constant coefficient. Consequently, new auxiliary variables need to be constructed to suitably handle the transformed equivalent free energy functional. It is remarkable that this specific model has been numerically studied using the IEQ approach in our previous work [49]. However, the IEQ method proposed in [49] requires solving a linear system with variable coefficients, which can be computationally inefficient. In contrast, the temporal marching algorithm proposed in this paper only necessitates solving constant-coefficient elliptic equations, resulting in improved computational efficiency. Moreover, the IEQ approach given in [49] solely focused on the time marching algorithm, whereas our approach provides a fully discrete method that is applicable to complex surfaces. To the best of our knowledge, this paper presents the first algorithm for this particular model on a complex surface.

We adopt the more advanced version of the IEQ method, the so-called explicit IEQ (EIEQ) method, in which by introducing a nonlocal variable and designing a special but trivial ODE for it, the decoupling structure is achieved, see [54] for its application in a different crystal growth model on the regular geometric domain. The superiority of the EIEQ method is reflected that the scheme involved ultimately only requires the solution of some linear constant-coefficient equations with the fully decoupled structure at each time step, and is therefore highly efficient in practice. Subdivision-based IGA approach provides us with a good candidate for solving the phase-field model on complex surfaces. We successfully demonstrate the unity of employing subdivision basis functions to represent the geometry and simulate the dynamical behaviors of the phase-field. This framework fully reflects the advantage of our hybrid IGA-EIEQ strategy to treat complex surface phase-field models. Various numerical experiments are carried out to demonstrate the energy stability and the accuracy of the developed method.

The rest of this paper is organized as follows. In Section 2 we briefly describe some basic knowledge of surfaces. In Section 3, the phase-field model for homopolymer blends on the surface is presented. In Section 4, we describe the coupling scheme of the subdivision-based IGA method with the EIEQ method, then provide a second-order fully-discrete scheme as well as proof of the unconditional energy stability, and their decoupling implementation. In Section 5, we implement several numerical examples by using our coupling scheme. In Section 6, we give the concluding remarks.

2. Preliminaries

Assume $\mathcal{S} := \{\mathbf{x}(u^1,u^2) \in \mathbb{R}^3 : (u^1,u^2) \in \mathscr{D} \subset \mathbb{R}^2\}$ be a sufficiently smooth and orientable surface, where (u^1,u^2) is its parameterization. Denote $g_{\alpha\beta} = \langle \mathbf{x}_{u^\alpha}, \mathbf{x}_{u^\beta}\rangle$ with

$$\mathbf{x}_{u^\alpha} = \frac{\partial \mathbf{x}}{\partial u^\alpha}, \quad \mathbf{x}_{u^\alpha u^\beta} = \frac{\partial^2 \mathbf{x}}{\partial u^\alpha \partial u^\beta}, \quad \alpha,\beta = 1,2, \tag{2.1}$$

and the surface normal

$$\mathbf{n} = \frac{\mathbf{x}_{u^1} \times \mathbf{x}_{u^2}}{\|\mathbf{x}_{u^1} \times \mathbf{x}_{u^2}\|}, \tag{2.2}$$

where $\langle\cdot,\cdot\rangle$, $\cdot\times\cdot$ and $\|\cdot\|$ stand for the usual inner product, cross product and Euclidean norm in $\mathbb{R}^3$ respectively. We further denote $[g^{\alpha\beta}] = [g_{\alpha\beta}]^{-1}$ and $g = \det[g_{\alpha\beta}]$, then we introduce the following geometric differential operators of interest.

2.0.1. Tangential gradient operator

Suppose that $f \in C^1(\mathcal{S})$, where $C^1(\mathcal{S})$ stands for a function space consisting of C^1 smooth functions on $\mathcal{S}$, then the tangential gradient operator ∇_s acting on f is defined as

$$\nabla_s f = [\mathbf{x}_{u^1}, \mathbf{x}_{u^2}][g^{\alpha\beta}][f_{u^1}, f_{u^2}]^T \in \mathbb{R}^3. \tag{2.3}$$

For a vector-valued function $\mathbf{f} = [f_1,\ldots,f_k]^T \in C^1(\mathcal{S})^k$, the gradient ∇_s acting on $\mathbf{f}$ is defined as

$$\nabla_s \mathbf{f} = [\nabla_s f_1, \ldots, \nabla_s f_k] \in \mathbb{R}^{3\times k}.$$

2.0.2. Divergence operator

Let $\mathbf{v} \in [C^1(\mathcal{S})]^3$ be a smooth vector field on surface $\mathcal{S}$. Then the divergence operator div_s acting on $\mathbf{v}$ is defined as

$$\mathrm{div}_s(\mathbf{v}) = \frac{1}{\sqrt{g}}\left[\frac{\partial}{\partial u^1}, \frac{\partial}{\partial u^2}\right]\left[\sqrt{g}[g^{\alpha\beta}][\mathbf{x}_{u^1}, \mathbf{x}_{u^2}]^T\mathbf{v}\right]. \tag{2.4}$$

2.0.3. Laplace–Beltrami operator

Let $f \in C^2(\mathcal{S})$. Then the Laplace–Beltrami operator (LBO) Δ_s acting on f is defined as

$$\Delta_s f = \mathrm{div}_s(\nabla_s f). \tag{2.5}$$

2.0.4. Sobolev space on surface

Assume that $\mathcal{S}$ is a sufficiently smooth surface. For a given constant k and a function $f \in C^\infty(\mathcal{S})$, denote $\nabla^k f$ the kth order covariant derivative of function f, with the convention $\nabla^0 f = f$. Let

$$C_k(\mathcal{S}) = \left\{ f \in C^\infty(\mathcal{S}) : \int_s |\nabla^j f|^2 \mathrm{d}\mathbf{x} \le \infty \text{ for } j = 0,\ldots,k \right\}.$$

Let $\mathcal{S}$ be a compact surface with at least kth order smoothness Sobolev space $H^k(\mathcal{S})$, which is the completion of $C_k(\mathcal{S})$ in the sense of norm

$$\|f\|_{H^k(\mathcal{S})} := \left(\sum_{j=0}^{k}\int_s |\nabla^j f|^2 \mathrm{d}\mathbf{x}\right)^{1/2}. \tag{2.6}$$

There hold the following two inner products on the surface $\mathcal{S}$, for $\xi, \rho \in H^1(\mathcal{S})$, that

$$(\xi,\rho) = \int_s \xi\rho \,\mathrm{d}\mathbf{x}, \quad \text{and} \quad (\nabla_s\xi, \nabla_s\rho) = \int_s \nabla_s\xi\cdot\nabla_s\rho \,\mathrm{d}\mathbf{x}.$$

3. Phase-field model of homopolymer blends on the surface

The phase-field model of homopolymer blends describes a homopolymer blend with the symmetric property, which is composed of molecules of component I and II. We use ϕ_0 to denote the average volume fraction of component I of the mixture, then the system state of the mixture is represented by $\phi(\mathbf{x},t)$ for every point $\mathbf{x} \in \mathcal{S}$ at the time t. The change of $\phi(\mathbf{x},t)$ with the time related to the local current $J_l(\mathbf{x})$ of component I can be represented by the following phenomenological mesoscopic dynamic equation [4–6]:

$$\phi_t = -\nabla_s \cdot J_l(\mathbf{x}). \tag{3.1}$$

Note that the transport of (3.1) follows the difference of the chemical potential. If there exists a linear relation between the gradient of the local chemical potential $\rho(\mathbf{x},t)$ and the local current $J_l(\mathbf{x},t)$ [55], the flux J_l is driven by

$$J_l(\mathbf{x},t) = -\lambda\nabla_s\rho(\mathbf{x},t), \tag{3.2}$$

where λ denotes the Onsager mobility coefficient. $\rho(\mathbf{x},t)$ is denoted as the functional derivative of a coarse-grained free energy functional $E(\phi)$, which reads as

$$\rho(\mathbf{x},t) = \frac{\delta E(\phi)}{\delta\phi}, \tag{3.3}$$

with

$$E(\phi) = \int_{\mathcal{S}}\left(\frac{\nu\alpha^2}{36}k(\phi)|\nabla_s\phi|^2 + F(\phi)\right)\mathrm{d}\mathbf{x}, \tag{3.4}$$

where α is the Kuhn segment length (cf. [6]), and

$$k(\phi) = \frac{1}{\phi(1-\phi)} \tag{3.5}$$

is the gradient energy coefficient of the de-Gennes type. The term $F(\phi)$ is called the bulk free energy of the mixture, and has the following form of the phase-field model of homopolymer blends

$$F(\phi) = \frac{1}{N\nu}(\phi\ln\phi + (1-\phi)\ln(1-\phi)) + \chi\phi(1-\phi), \tag{3.6}$$

where the coefficient N is the degree of the polymerization of the chains, the coefficient ν is the volume of one repeat unit (monomer), and the coefficient χ is the Flory–Huggins type interaction parameter (cf. [6]).

Denote $M = \frac{\Lambda}{\nu N}, \varepsilon^2 = \frac{\nu^2\alpha^2 N}{36}$ and $\beta = \chi\nu N$, we can numerically solve the phase-field model of homopolymer blends according to the following scaled equation form

$$\phi_t = M\Delta_s\mu, \tag{3.7}$$

$$\mu = \frac{\delta E}{\delta\phi} = -2\varepsilon^2\nabla_s\cdot(k(\phi)\nabla_s\phi) + \varepsilon^2 k'(\phi)|\nabla_s\phi|^2 + f(\phi), \tag{3.8}$$

where

$$\begin{cases} k'(\phi) = \dfrac{(2\phi-1)}{\phi^2(1-\phi)^2}, \\ F(\phi) = \phi\ln\phi + (1-\phi)\ln(1-\phi) + \beta(\phi-\phi^2), \\ f(\phi) = F'(\phi) = \ln(\dfrac{\phi}{1-\phi}) + \beta(1-2\phi). \end{cases} \tag{3.9}$$

For simplicity, we only consider closed surface domains in this paper so that we ignore all complex boundary conditions.

By taking the L^2 inner products of (3.7) with $-\mu$, of (3.8) with ϕ_t, and performing the integration by parts, we get

$$-(\phi_t,\mu) = M\|\nabla_s\mu\|^2, \tag{3.10}$$

and

$$\begin{aligned}(\mu, \phi_t) &= 2\varepsilon^2(k(\phi)\nabla_s\phi, \nabla_s\phi_t) + \varepsilon^2(k'(\phi)|\nabla_s\phi|^2, \phi_t) + (f(\phi), \phi_t)\\ &= \varepsilon^2(k(\phi), \partial_t|\nabla_s\phi|^2) + \varepsilon^2(|\nabla_s\phi|^2, \partial_t k(\phi)) + (f(\phi), \phi_t)\\ &= \frac{d}{dt}(\varepsilon^2 k(\phi), |\nabla_s\phi|^2) + \frac{d}{dt}(F(\phi), 1).\end{aligned} \tag{3.11}$$

Then taking the sum of the above equations, we obtain the energy dissipation law

$$\frac{d}{dt}E(\phi) = -M\|\nabla_s\mu\|^2 \le 0, \tag{3.12}$$

where

$$E(\phi) = \int_{\mathcal{S}} \left(\varepsilon^2 k(\phi)|\nabla_s\phi|^2 + F(\phi)\right) \mathrm{d}\mathbf{x}. \tag{3.13}$$

We aim at constructing a fully-discrete scheme to solve the phase-field model of homopolymer blends (3.7)–(3.8) on the surface that accords with the discrete form of the continuous energy law (3.12). The main challenge we face is how to discretize the nonlinear terms resulting from the energy functionals, i.e., the Flory–Huggins type potential term $f(\phi)$ and the gradient entropy term $k(\phi)$ with the de-Gennes type coefficient.

4. IGA-EIEQ scheme on the surface

The constructed numerical algorithm must ensure that the free energy is within an open domain (0, 1). As for the bulk free energy $F(\phi)$ and the gradient entropy $k(\phi)$ in the free energy functional (3.4), we use C^2 continuous convex piecewise functions to regularize them from (0, 1) to $(-\infty, \infty)$. About the bulk free energy $F(\phi)$, for any $\sigma > 0$, we rewrite it as [56]

$$F(\phi) = \mathcal{F}(\phi) + \beta(\phi - \phi^2), \tag{4.1}$$

with

$$\mathcal{F}(\phi) = \begin{cases} \phi\ln\phi + \dfrac{(1-\phi)^2}{2\sigma} + (1-\phi)\ln\sigma - \dfrac{\sigma}{2}, & \text{if } \phi \ge 1-\sigma,\\ \phi\ln\phi + (1-\phi)\ln(1-\phi), & \text{if } \sigma \le \phi \le 1-\sigma,\\ (1-\phi)\ln(1-\phi) + \dfrac{\phi^2}{2\sigma} + \phi\ln\sigma - \dfrac{\sigma}{2}, & \text{if } \phi \le \sigma. \end{cases} \tag{4.2}$$

For the other gradient entropy $k(\phi)$, we change it as

$$k(\phi) = \begin{cases} \dfrac{1}{\sigma(1-\sigma)} + \dfrac{1-2\sigma}{(1-\sigma)^2\sigma^2}(\phi - (1-\sigma)), & \text{if } \phi \ge 1-\sigma,\\ \dfrac{1}{\phi(1-\phi)}, & \text{if } \sigma \le \phi \le 1-\sigma,\\ \dfrac{1}{\sigma(1-\sigma)} + \dfrac{2\sigma-1}{(1-\sigma)^2\sigma^2}(\phi - \sigma), & \text{if } \phi \le \sigma. \end{cases} \tag{4.3}$$

In the following section, we introduce our numerical algorithm which combines the EIEQ approach and recently developed subdivision-based IGA method to construct a second-order discrete scheme with unconditional energy stability.

4.1. EIEQ time advancing strategy

An ideal time discretization method requires the properties of the linearity and unconditional energy stability. For the transformed system (3.7)–(3.8), the key step of the EIEQ methodology is to design two new variables, one of which can "quadratize" the nonlinear terms, and the other of which can be used to achieve the decoupling calculation. After that, our decoupled scheme is linear, second-order time-accurate and unconditional energy stable. Our final task is to solve several elliptic equations with constant-coefficient. Next, we describe the detailed idea.

The effect of the first new variable U is to quadratize the energy potential, which defined as

$$U(\phi) = \sqrt{\varepsilon^2(k(\phi) - C)|\nabla_s\phi|^2 + F(\phi) - \frac{\eta}{2}\phi^2 + B}. \tag{4.4}$$

It is easy to see that we need predefine two positive constants η and B, where the function of constant B is to ensure the term in the square root always positive since the negative quadratic term related to η can be always bounded from below. With the help of the new variable U, we can change the model (3.7)–(3.8) into the following equivalent formulation:

$$\phi_t = M\Delta_s\mu, \tag{4.5}$$

$$\mu = -2C\varepsilon^2\Delta_s\phi + \eta\phi + HU, \tag{4.6}$$

$$U_t = \frac{1}{2}H\phi_t, \tag{4.7}$$

where the emerging variable H is

$$\begin{aligned}H &= 2\frac{d}{d\phi}U(\phi)\\ &= \frac{-2\varepsilon^2\nabla\cdot((k(\phi)-C)\nabla_s\phi) + \varepsilon^2 k'(\phi)|\nabla_s\phi|^2 + f(\phi) - \eta\phi}{\sqrt{\varepsilon^2(k(\phi)-C)|\nabla_s\phi|^2 + F(\phi) - \frac{\eta}{2}\phi^2 + B}}.\end{aligned} \tag{4.8}$$

The other of the nonlocal variable $Q(t)$ is used to achieve the decoupling calculation, where we relate this variable to an ODE system as

$$\begin{cases} Q(t) = (HU, \phi_t) - (H\phi_t, U),\\ Q|_{t=0} = 1. \end{cases} \tag{4.9}$$

$Q(t)$ is equal to 1 since $Q_t = 0$ and $Q|_{t=0} = 1$.

After that, with these two newly constructed variables U and $Q(t)$ with the dependent ODE (4.9), the phase-field model of homopolymer blends (3.7)–(3.8) is reformulated as:

$$\phi_t = M\Delta_s\mu, \tag{4.10}$$

$$\mu = -2C\varepsilon^2\Delta_s\phi + \eta\phi + QHU, \tag{4.11}$$

$$U_t = \frac{1}{2}QH\phi_t, \tag{4.12}$$

$$Q_t = (HU, \phi_t) - (H\phi_t, U), \tag{4.13}$$

with the initial condition

$$\begin{cases} \phi|_{t=0} = \phi_0,\\ \mu|_{t=0} = -2\varepsilon^2\nabla_s\cdot(k(\phi_0)\nabla_s\phi_0) + \varepsilon^2 k'(\phi_0)|\nabla_s\phi_0|^2 + f(\phi_0),\\ U|_{t=0} = \sqrt{\varepsilon^2(k(\phi_0)-C)|\nabla_s\phi_0|^2 + F(\phi_0) - \frac{\eta}{2}\phi_0^2 + B}. \end{cases} \tag{4.14}$$

Remark 4.1. The two newly obtained systems (4.5)–(4.7) and (4.10)–(4.13) through the transforming method using some new constructed variables are equivalent to the initial system (3.7)–(3.8) because we can recover the previous system from the latter system through several integral operation over time. For example, (4.4) can be recovered if we integrate the Eqs. (4.7) over time with the given initial conditions (4.14). In addition, it is easy to see the equivalence between the new system (4.10)–(4.13) and the system (4.5)–(4.7) because $Q \equiv 1$.

Theorem 4.1. *The transformed equivalent system (4.10)–(4.13) guarantees the law of the energy dissipation*

$$\frac{d}{dt}\tilde{E}(\phi, Q, U) = -M\|\nabla_s \mu\|^2 \leq 0, \tag{4.15}$$

where the energy functional

$$\tilde{E}(\phi, Q, U) = \int_{\mathcal{S}} \left(C\varepsilon^2 |\nabla_{\mathcal{S}}\phi|^2 + \frac{\eta}{2}|\phi|^2 + U^2 - B \right) \mathrm{d}x + \frac{1}{2}|Q|^2 - \frac{1}{2}. \tag{4.16}$$

Proof. By taking the L^2 inner product of (4.10) with $-\mu$, of (4.11) with ϕ_t, of (4.12) with $2U$, of (4.13) with Q, and perform the integration by parts, we get

$$-(\phi_t, \mu) = M(\nabla_s \mu, \nabla_s \mu), \tag{4.17}$$

$$(\mu, \phi_t) = 2C\varepsilon^2(\nabla_s \phi, \nabla_s \phi_t) + \eta(\phi, \phi_t) + Q(HU, \phi_t), \tag{4.18}$$

$$2(U_t, U) = Q(H\phi_t, U), \tag{4.19}$$

$$\frac{d}{dt}\left(\frac{1}{2}|Q|^2\right) = Q(HU, \phi_t) - Q(H\phi_t, U). \tag{4.20}$$

After taking the sum of (4.17)–(4.20), we obtain the law of the energy dissipation (4.15).

The energy law (4.15) of the transformed system (4.10)–(4.13) is exactly the same as the energy law (3.12) for the original system (3.7)–(3.8) in the time continuous case. On the basis of the current energy dissipation law (4.15), we describe the spatiotemporal fully-discrete scheme for the corresponding system (4.10)–(4.13).

4.2. Subdivision-based IGA method

Subdivision is a popular technique, which is widely applied to represent smooth models in the area of engineering design. It provides us with an efficient and compact description of the model interest with certain smoothness. Subdivision approach has the flexibility and the freedom of treating complex surface models with any topology structure, moreover it the exactly expressible properties for geometries which can be guaranteed no change along with the parameterization process. Actually, the refinement process of the subdivision approach is equivalent to the h-refinement of NURBS. Different from traditional spline approaches, subdivision representation has no requirement of the complex continuity constraints cross patches.

Starting from an initial coarse mesh, or called control mesh, we can obtain a smooth surface by the Loop subdivision scheme

$$\mathbf{x}^j = S_{j-1}^j \mathbf{x}^{j-1}, \tag{4.21}$$

where we denote S_{j-1}^j as the global subdivision operation from level $j-1$ to level j. The entries of the sparse matrix S_{j-1}^j are dependent of the topology of the mesh and its corresponding subdivision weight coefficients. We can update the new place of the control point by the old point with weight $\alpha = 1 - n\beta$ and all 1-ring surrounding control points with weight $\beta = \frac{1}{n}\left[\frac{5}{8} - \left(\frac{3}{8} + \frac{1}{4}\cos\frac{2\pi}{n}\right)^2\right]$, where n is the valence of the control point (see Fig. 4.1 (*a*)). Then we can achieve a new point at each edge by averaging the four adjacent points (see Fig. 4.1 (*b*)). Repeated refinement leads to hierarchical and increasingly refined models, which finally generate the limit surface with C^1 smoothness.

Assume that we denote the initial control mesh as Ω_h^0, and the subsequent series of the control meshes as Ω_h^k, $k = 0, \ldots, \infty$, through repeated Loop subdivision. A limit surface $\mathcal{S}$ can be achieved through an infinite subdivision procedure as $k \to \infty$.

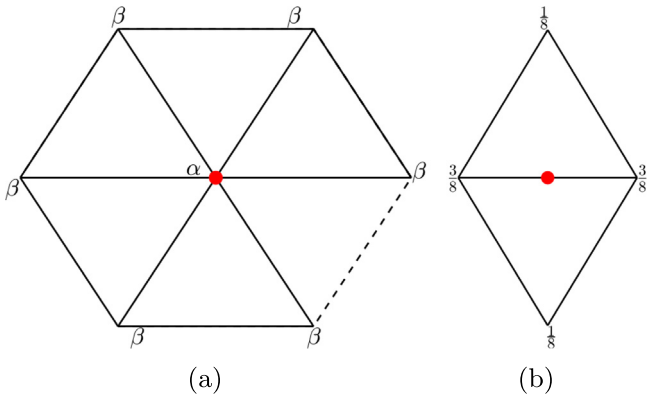

Fig. 4.1. (a) Vertex refinement rule, $\alpha = 1 - n\beta$, where $\beta = \frac{1}{n}\left[\frac{5}{8} - \left(\frac{3}{8} + \frac{1}{4}\cos\frac{2\pi}{n}\right)^2\right]$, and n is the valence of the control vertex. (b) Edge refinement rule.

Every control point $\mathbf{x}_0^k$ of valence n on the mesh Ω_h^k and its 1-ring adjacent points $\mathbf{x}_j^k, j = 1, 2, \ldots, n$, will converge to a clear location under the condition of the parameter $\beta \in (-3/8n, 13/8n)$, which is stated as the following Lemma 4.1.

Lemma 4.1. *Let $\mathbf{x}_0^k$ be a control point of valence n on the mesh Ω_h^k, and $\mathbf{x}_j^k, j = 1, \ldots, n$, be its 1-ring adjacent control points. All these points converge to a single position*

$$\hat{\mathbf{x}}_0 = (1 - nl)\mathbf{x}_0^k + l\sum_{j=1}^{n} \mathbf{x}_j^k, \quad l = \frac{1}{n + 3/(8\beta)}, \tag{4.22}$$

as the subdivision step $k \to \infty$ (see [32] for the proof).

We can use the subdivision shape functions to represent the solution of high-order PDEs governing the dynamical behaviors of complex geometry with any topological structures, which are C^1 continuity or H^2 integrability. The subdivision model represents complicated interest domain and simulates its physical property through the same set of formulas. We can get a reliable and exact computation in the processing of the finite element integration through the computation of Loop basis functions and their derivatives at arbitrary parameter positions for every triangular patch.

For a regular patch which means the valence of all control points of the triangular patch is six, we can exactly describe it by a quartic box-spline as

$$\mathbf{x}(u, v) = \sum_{i=1}^{12} B_i(u, v)\mathbf{x}_i^k, \tag{4.23}$$

where $(u, v, 1 - u - v)$ is the barycentric coordinates of the parametric patch, $\mathbf{x}_i^k$ are the corresponding 2-ring surrounding neighbor control points of the control mesh (see Fig. 4.2(a)), and B_i are the quartic box-splines (see their analytic expression in [57]). Then we can determine any points lying within the regular patch directly using the set of the box spline basis functions. For an irregular patch which means the valence of at least one control point for this patch is not six, there has no explicitly computable formula for it. However, the quartic box-spline form (4.23) is still used to calculate the resulting limit surface patch through a fast algorithm proposed by Stam [57]. The core idea is to subdivide repeatedly this patch until the position you need to calculate is included in a quartic box-spline patch (see Fig. 4.2(b)).

The finite element integration is performed at several Gauss points within every parametric patch, where the Loop basis functions have the 2-ring of triangles support. In order to make

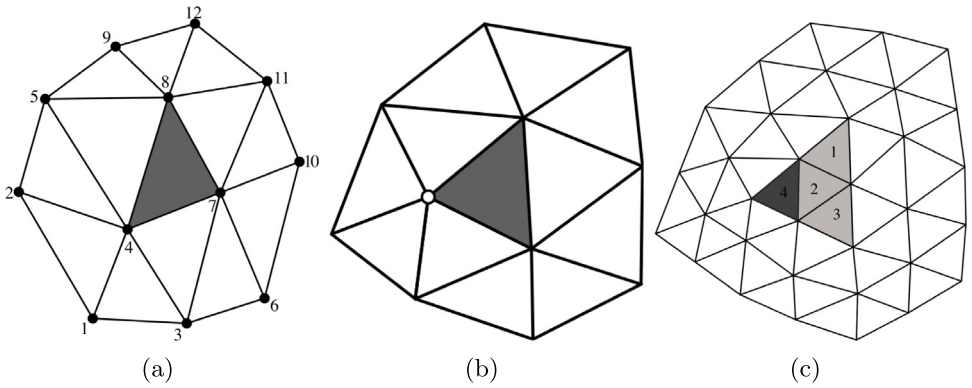

Fig. 4.2. (a): A regular computable Loop subdivision patch. The shaded patch is the computable Loop subdivision patch with its surrounding 12 control points. (b) and (c): An irregular Loop subdivision patch. The extraordinary control point marked as a hollow ring. Subdividing this patch once can generate three computable sub-patches marked as 1, 2 and 3, and one uncomputable sub-patch marked as 4. This uncomputable patch can be repeatedly subdivided to generate more computable sub-patches.

sure that the quadrature computation arrives at the necessary precision, very limited subdivision steps should be performed to make all of the hierarchical limit patches become computable quartic box-splines patches. To reduce the computation expenditure, we develop a simplified approach of adaptive discretization subdivision, where the basic idea is to replace the refinement of mesh patches with the refinement of basis functions (see [37]).

The general process of solving the governing equations is to transform the variables into linear combinations of finite element basis functions with compact support. We demonstrate the unity of employing Loop subdivision basis functions to represent the surface geometry and perform the finite element simulation of the phase-field movement on the surface. Assume the set of basis functions to be $\phi_1, \ldots, \phi_n$ in the finite element function space $H^2(\mathcal{S}_h)$, where the control mesh $\mathcal{S}_h$ of the limit form of Loop subdivision has n control points $\mathbf{x}_1, \ldots, \mathbf{x}_n$.

Loop basis functions make up a partition of unity, and have the same superior properties as classical finite elements. Firstly, they are nonnegative everywhere and positive around their corresponding control points because the weight coefficients of the subdivision schemes are positive. Secondly, the limit position of each control point $\mathbf{x}_j$ is a linear summation of itself and its one-ring neighboring control points so that the support of each basis function has two-ring neighborhoods. Finally, the weight coefficients of all subdivision schemes are summed to one, therefore we have $\sum_{j=0}^{m} \phi_j = 1$.

4.3. Fully-discrete scheme

In this subsection, we describe its second-order spatiotemporal fully-discrete scheme, the unconditional energy stability, and the decoupling implement process. In the following context, the time step size is denoted as $\delta t > 0$ where $t^n = n\delta t$ and $0 \le n \le N = [T/\delta t]$. We take the test functions θ_h, ϑ_h and ζ_h in the finite element space $H^2(\mathcal{S}_h)$ deduced by the limit form of the Loop subdivision as described in Section 4.2.

We already know ϕ_h^n, μ_h^n, U_h^n and ϕ_h^{n-1}, μ_h^{n-1}, U_h^{n-1}, for $n \ge 1$, then we need achieve ϕ_h^{n+1}, μ_h^{n+1}, U_h^{n+1} using the following second-order scheme based on the backward difference formula:

$$\left(\frac{3\phi_h^{n+1} - 4\phi_h^n + \phi_h^{n-1}}{2\delta t}, \theta_h\right) = -M(\nabla_s \mu_h^{n+1}, \nabla_s \theta_h), \tag{4.24}$$

$$(\mu_h^{n+1}, \vartheta_h) = 2C\varepsilon^2(\nabla_s \phi_h^{n+1}, \nabla_s \vartheta_h) + \eta(\phi_h^{n+1}, \vartheta_h) + Q^{n+1}(H_h^* U_h^*, \vartheta_h), \tag{4.25}$$

$$\left(\frac{3U_h^{n+1} - 4U_h^n + U_h^{n-1}}{2\delta t}, \zeta_h\right) = \frac{1}{2} Q^{n+1}\left(H_h^* \phi_{ht}^*, \zeta_h\right), \tag{4.26}$$

$$\frac{3Q^{n+1} - 4Q^n + Q^{n-1}}{2\delta t} = (H_h^* U_h^*, \frac{3\phi_h^{n+1} - 4\phi_h^n + \phi_h^{n-1}}{2\delta t}) - (H_h^* \phi_{ht}^*, U_h^{n+1}), \tag{4.27}$$

where the known terms ϕ_h^*, U_h^*, H_h^* and ϕ_{ht}^* are

$$\begin{cases} \phi_h^* = 2\phi_h^n - \phi_h^{n-1}, \ U_h^* = 2U_h^n - U_h^{n-1}, \\ H_h^* = H(\phi_h^*), \ \phi_{ht}^* = \frac{5\phi_h^n - 8\phi_h^{n-1} + 3\phi_h^{n-2}}{2\delta t}. \end{cases} \tag{4.28}$$

Its corresponding unconditional energy stability is described as the following Theorem 4.2.

Theorem 4.2. *The second-order scheme (4.24)–(4.27) is unconditionally energy stable, i.e., satisfies the following discrete energy dissipation law:*

$$\frac{\tilde{E}^{n+1} - \tilde{E}^n}{\delta t} \le -M\|\nabla_s \mu_h^{n+1}\|^2, \tag{4.29}$$

where, for an integer $k \ge 0$, the discrete-form energy $\tilde{E}^k$ is defined as

$$\begin{aligned} \tilde{E}^k = \ & C\varepsilon^2(\|\nabla_s \phi_h^k\|^2 + \|2\nabla_s \phi_h^k - \nabla_s \phi_h^{k-1}\|^2) \\ & + \frac{\eta}{2}(\|\phi_h^k\|^2 + \|2\phi_h^k - \phi_h^{k-1}\|^2) \\ & + (\|U_h^k\|^2 + \|2U_h^k - U_h^{k-1}\|^2) + \frac{1}{2}(|Q^k|^2 + |2Q^k - Q^{k-1}|^2). \end{aligned} \tag{4.30}$$

Proof. Firstly we take $\theta_h = -\mu_h^{n+1}$ in (4.24) and perform the integration by parts, we get

$$-\left(\frac{3\phi_h^{n+1} - 4\phi_h^n + \phi_h^{n-1}}{2\delta t}, \mu_h^{n+1}\right) = M\|\nabla_s \mu_h^{n+1}\|^2. \tag{4.31}$$

By taking $\vartheta_h = \frac{3\phi_h^{n+1} - 4\phi_h^n + \phi_h^{n-1}}{2\delta t}$ in (4.25), using the following identity of

$$2(3a-4b+c, a) = a^2 - b^2 + (2a-b)^2 - (2b-c)^2 + (a-2b+c)^2, \tag{4.32}$$

and performing the integration by parts, we derive

$$\begin{aligned}&\left(\mu_h^{n+1}, \tfrac{3\phi_h^{n+1}-4\phi_h^n+\phi_h^{n-1}}{2\delta t}\right)\\&=\frac{C\varepsilon^2}{2\delta t}(\|\nabla_s\phi_h^{n+1}\|^2-\|\nabla_s\phi_h^n\|^2+\|2\nabla_s\phi_h^{n+1}-\nabla_s\phi_h^n\|^2\\&-\|2\nabla_s\phi_h^n-\nabla_s\phi_h^{n-1}\|^2+\|\nabla_s\phi_h^{n+1}-2\nabla_s\phi_h^n+\nabla_s\phi_h^{n-1}\|^2)\\&+\frac{\eta}{4\delta t}(\|\phi_h^{n+1}\|^2-\|\phi_h^n\|^2+\|2\phi_h^{n+1}-\phi_h^n\|^2\\&-\|2\phi_h^n-\phi_h^{n-1}\|^2+\|\phi_h^{n+1}-2\phi_h^n+\phi_h^{n-1}\|^2)\\&+Q^{n+1}(H_h^*U_h^*, \tfrac{3\phi_h^{n+1}-4\phi_h^n+\phi_h^{n-1}}{2\delta t}).\end{aligned}\tag{4.33}$$

By taking $\zeta_h = 2U_h^{n+1}$ in (4.26) and using (4.32), we get

$$\begin{aligned}&\frac{1}{2\delta t}(\|U_h^{n+1}\|^2-\|U_h^n\|^2+\|2U_h^{n+1}-U_h^n\|^2-\|2U_h^n-U_h^{n-1}\|^2\\&+\|U_h^{n+1}-2U_h^n+U_h^{n-1}\|^2)=Q^{n+1}(H_h^*\phi_{ht}^*, U_h^{n+1}).\end{aligned}\tag{4.34}$$

By multiplying (4.27) with Q^{n+1} and using (4.32), we obtain

$$\begin{aligned}&\frac{1}{4\delta t}(3Q^{n+1}-4Q^n+Q^{n-1})Q^{n+1}\\&=Q^{n+1}(H_h^*U_h^*, \tfrac{3\phi_h^{n+1}-4\phi_h^n+\phi_h^{n-1}}{2\delta t})-Q^{n+1}(H_h^*\phi_{ht}^*, U_h^{n+1}).\end{aligned}\tag{4.35}$$

By taking the sum of (4.31), (4.33), (4.34) and (4.35), and using (4.32) for the left hand of (4.35), we have

$$\begin{aligned}&\frac{C\varepsilon^2}{2\delta t}(\|\nabla_s\phi_h^{n+1}\|^2-\|\nabla_s\phi_h^n\|^2+\|2\nabla_s\phi_h^{n+1}-\nabla_s\phi_h^n\|^2\\&-\|2\nabla_s\phi_h^n-\nabla_s\phi_h^{n-1}\|^2\\&+\|\nabla_s\phi_h^{n+1}-2\nabla_s\phi_h^n+\nabla_s\phi_h^{n-1}\|^2)\\&+\frac{\eta}{4\delta t}(\|\phi_h^{n+1}\|^2-\|\phi_h^n\|^2+\|2\phi_h^{n+1}-\phi_h^n\|^2-\|2\phi_h^n-\phi_h^{n-1}\|^2\\&+\|\phi_h^{n+1}-2\phi_h^n+\phi_h^{n-1}\|^2)\\&+\frac{1}{2\delta t}(\|U_h^{n+1}\|^2-\|U_h^n\|^2+\|2U_h^{n+1}-U_h^n\|^2-\|2U_h^n-U_h^{n-1}\|^2\\&+\|U_h^{n+1}-2U_h^n+U_h^{n-1}\|^2)\\&+\frac{1}{4\delta t}(|Q^{n+1}|^2-|Q^n|^2+|2Q^{n+1}-Q^n|^2-|2Q^n-Q^{n-1}|^2\\&+|Q^{n+1}-2Q^n+Q^{n-1}|^2)\\&=-M\|\nabla_{\mathcal{S}}w_h^{n+1}\|^2,\end{aligned}$$

which implies the energy stability (4.29) is true after we ignore its some positive terms.

4.3.1. Decoupled calculation

We introduce a nonlocal splitting method to obtain the decoupling calculation for (4.24)–(4.27).

Step 1: We split ϕ_h^{n+1}, μ_h^{n+1} and U_h^{n+1} into the linear combination forms as

$$\begin{aligned}\phi_h^{n+1}&=\phi_{1h}^{n+1}+Q^{n+1}\phi_{2h}^{n+1},\ \mu_h^{n+1}=\mu_{1h}^{n+1}+Q^{n+1}\mu_{2h}^{n+1},\ U_h^{n+1}\\&=U_{1h}^{n+1}+Q^{n+1}U_{2h,}^{n+1}\end{aligned}\tag{4.36}$$

we solve ϕ_{ih}^{n+1}, μ_h^{n+1} and U_{ih}^{n+1}, $i=1,2$, as follows.

Using (4.36), we replace ϕ_h^{n+1}, μ_h^{n+1} and U_h^{n+1} of the system (4.24)–(4.26), and decompose the obtained equations into the following four systems:

$$\begin{cases}(\frac{3\phi_{1h}^{n+1}-4\phi_h^n+\phi_h^{n-1}}{2\delta t}, \theta_h)=-M(\nabla_s\mu_{1h}^{n+1}, \nabla_s\theta_h),\\(\mu_{1h}^{n+1}, \vartheta_h)=2C\varepsilon^2(\nabla_s\phi_{1h}^{n+1}, \nabla_s\vartheta_h)+\eta(\phi_{1h}^{n+1}, \vartheta_h),\end{cases}\tag{4.37}$$

$$\begin{cases}(\frac{3\phi_{2h}^{n+1}}{2\delta t}, \theta_h)=-M(\nabla_s\mu_{2h}^{n+1}, \nabla_s\theta_h),\\(\mu_{2h}^{n+1}, \vartheta_h)=2C\varepsilon^2(\nabla_s\phi_{2h}^{n+1}, \nabla_s\vartheta_h)+\eta(\phi_{2h}^{n+1}, \vartheta_h)+(H_h^*U_h^*, \vartheta_h),\end{cases}\tag{4.38}$$

$$(\frac{3U_{1h}^{n+1}}{2\delta t}, \zeta_h)=(\frac{4U_h^n-U_h^{n-1}}{2\delta t}, \zeta_h),\tag{4.39}$$

$$(\frac{3U_{2h}^{n+1}}{2\delta t}, \zeta_h)=\frac{1}{2}(H_h^*\phi_{ht}^*, \zeta_h).\tag{4.40}$$

The system (4.37) and (4.38) is easy to be solved because there are linear elliptic with constant coefficients. (4.39) and (4.40) are also very easy to be solved.

Step 2: By using the obtained values of ϕ_{1h}^{n+1}, ϕ_{2h}^{n+1}, and U_{1h}^{n+1}, U_{2h}^{n+1} by solving (4.37)–(4.40), we update Q^{n+1} in (4.27) through

$$\left(\frac{3}{2\delta t}-\gamma_2\right)Q^{n+1}=\frac{1}{2\delta t}(4Q^n-Q^{n-1})+\gamma_1,\tag{4.41}$$

where γ_1 and γ_2 are given as

$$\begin{cases}\gamma_1=(H_h^*U_h^*, \frac{3\phi_{1h}^{n+1}-4\phi_h^n+\phi_h^{n-1}}{2\delta t})-(H_h^*\phi_{ht}^*, U_{1h}^{n+1}),\\\gamma_2=(H_h^*U_h^*, \frac{3\phi_{2h}^{n+1}}{2\delta t})-(H_h^*\phi_{ht}^*, U_{2h}^{n+1}),\end{cases}\tag{4.42}$$

and H_h^*, U_h^* and ϕ_{ht}^* are given in (4.28).

Finally, we need prove the solvability of Q in (4.41) through showing the coefficient $\frac{3}{2\delta t}-\gamma_2\neq 0$. By taking $\theta_h=\mu_{2h}^{n+1}$ and $\vartheta_h=\frac{3}{2\delta t}\phi_{2h}^{n+1}$ in (4.38), we get

$$\begin{aligned}&M\left\|\nabla_s\mu_{2h}^{n+1}\right\|^2+\frac{3C\varepsilon^2}{\delta t}\left\|\nabla_s\phi_{2h}^{n+1}\right\|^2+\frac{3\eta}{2\delta t}\left\|\phi_{2h}^{n+1}\right\|^2\\&=-(H_h^*U_h^*, \frac{3\phi_{2h}^{n+1}}{2\delta t}),\end{aligned}\tag{4.43}$$

then choosing $\zeta_h=2U_{2h}^{n+1}$ in (4.40), we obtain

$$\left\|\frac{3U_{2h}^{n+1}}{\delta t}\right\|^2=(H_h^*\phi_h^*, U_{2h}^{n+1}).\tag{4.44}$$

We can get $-\gamma_2\geq 0$ by taking the sum of (4.43) and (4.44). Thus (4.41) is always solvable.

We implement the decoupled calculation for the discrete scheme. As we can see that we do not introduce any additional solution steps for the nonlinear terms. The indispensable computation is that several elliptic equations with constant coefficients are solved at each time step.

5. Numerical examples

In this section, some practical simulations are carried out to validate the efficiency, accuracy, and energy stability of this coupling discrete scheme. The solution surface regions for the numerical experiments result from the limit process of the Loop subdivision. Similar to the classical FEM, the Gaussian integral calculation is carried out on each patch of the triangular discretization for the limit surface. The linear system of the fully discretization scheme for the equation is highly sparse, we need a robust iterative method to solve them. In this paper, we adopt the GMRES solver, where we set the number of iterative steps long enough to obtain the proper convergence of the scheme.

5.1. Convergence test

We first test the convergence rate of this coupling scheme using a closed sphere with the unit radius, i.e.,

$$\mathcal{S}=\{(x,y,z):\sqrt{x^2+y^2+z^2}=1\}.\tag{5.1}$$

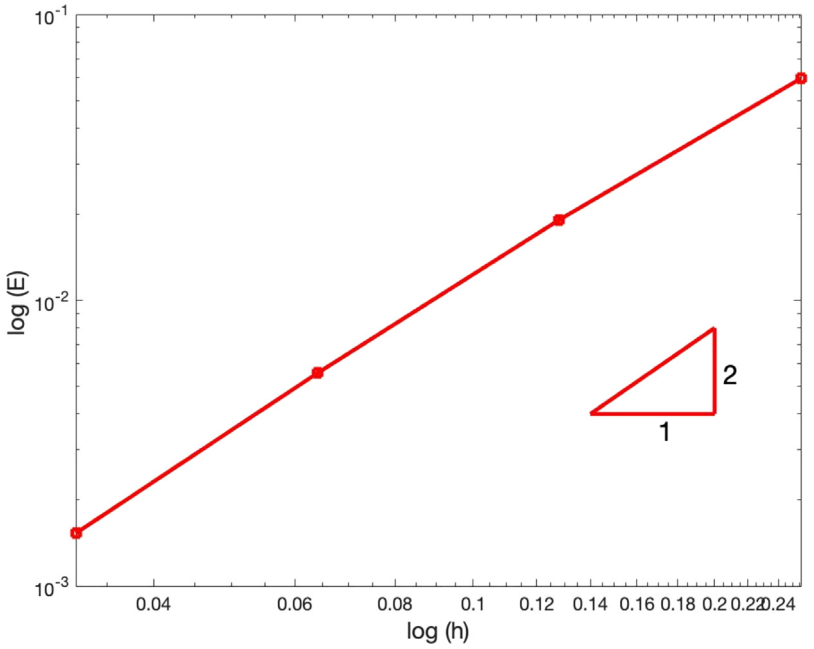

Fig. 5.1. Convergence rate of the phase-field model of homopolymer blends on the unit sphere.

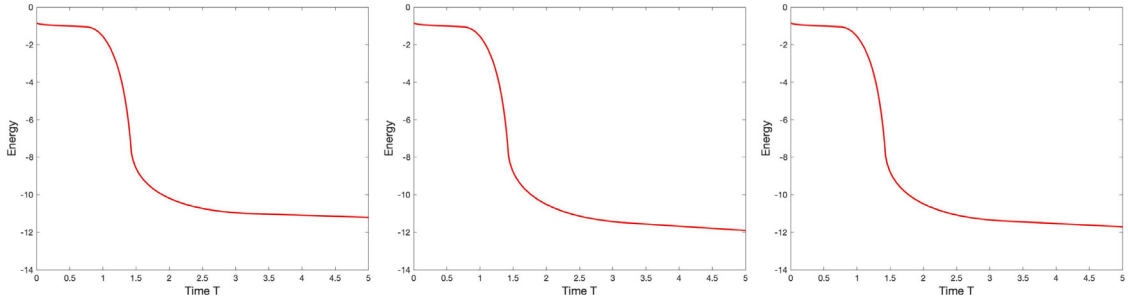

Fig. 5.2. Phase-field model of homopolymer blends for the sphere (5.5) with $\bar{\phi}_0 = 0.3$: Time evolution of the free functional for three different time step sizes $\delta t = 2e{-}3,\ 1e{-}3$ and $5e{-}4$, which are plotted in (a), (b) and (c) respectively. The energy curves decay for the three different time step sizes, which shows our coupling scheme is unconditionally stable.

The parameters of the system are given as

$$M = 1,\ \beta = 2.5,\ \varepsilon = 1e-2,$$
$$\sigma = 1e-4,\ C = 5e-1,\ \eta = 4,\ B = 9e3, \tag{5.2}$$

and the initial condition is set as

$$\phi_0 = \sin(2x)\cos(3y) + 0.2. \tag{5.3}$$

To obtain the convergence rate, a series of the uniform meshes $\mathcal{S}_{h_i}$ from coarse to refined are performed, where the values of the vertex valence are in [4, 6], and h_i is the mesh size. Since the subdivision-based IGA method is second-order accurate (cf. [36]), we set the time step sizes $\delta t_i = Ch_i$ for the ith level surface mesh $\mathcal{S}_{h_i}$, where C is a given constant between 0 and 1. Because we do not know its exact solution, we choose the solution achieved with a very fine mesh size as the benchmark solution, which is used approximately as the exact solution for verifying the numerical errors. We plot the L^2 numerical error of the scheme in Fig. 5.1 when $t = 2.56e{-}1$, where the total number of patches/vertices for these surface models are 512/258, 2048/1026, 8192/4098, 32768/16386, and the corresponding mesh sizes $h_i = 0.2543,\ 0.1169,\ 0.0622,\ 0.0326$, respectively. We observe that the scheme is second-order accurate for space.

5.2. Spinodal decomposition on surfaces

We study the process of the phase separation by observing a homogeneous binary mixture. It is quenched into the unstable part of its miscibility gap, where the spinodal decomposition happens, then manifests in the spontaneous growth of the concentration fluctuations that leads the system from the homogeneous to the two-phase state. The domains of the binary components are formed and there appears the interface between them shortly after the phase separation starts. In this section, we represent the phase separation (spinodal decomposition) simulation on three different surface models under three different initial conditions (cf. [4,6,58–61]).

The initial condition read as

$$\phi_0 = \bar{\phi}_0 + 0.001\text{rand}(x, y, z), \tag{5.4}$$

and the rand(x, y, z) is the random number in $[-1, 1]$ with the zero mean.

The first surface domain is set as a closed sphere with the unit radius

$$\mathcal{S}_1 = \{(x, y, z) : x^2 + y^2 + z^2 = 1\}, \tag{5.5}$$

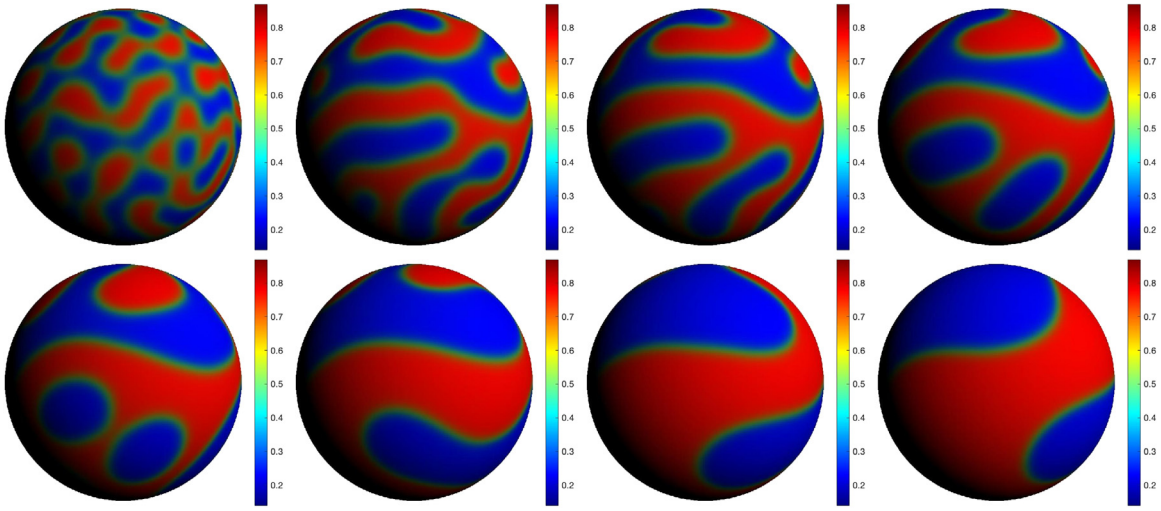

Fig. 5.3. Snapshots of the spinodal decomposition on the sphere (5.5) are taken at $t = 1.5, 2.5, 5, 10, 15, 25, 30, 40$, where the phase variable ϕ is chosen with the initial value $\bar{\phi}_0 = 0.5$, and the time step $\delta t = 1e{-}3$.

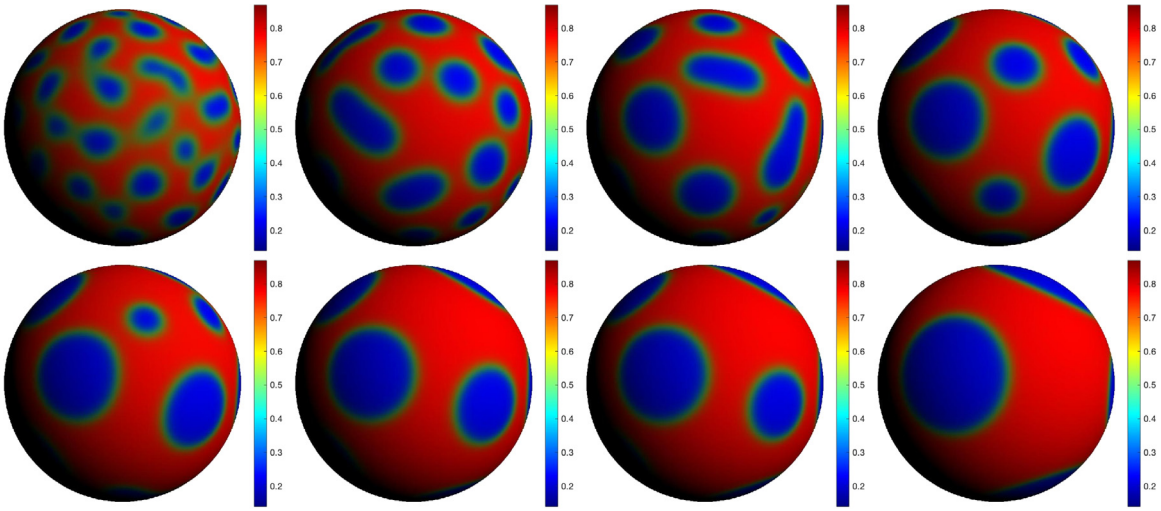

Fig. 5.4. Snapshots of the spinodal decomposition on the sphere (5.5) are taken at $t = 1.5, 3, 5, 10, 15, 20, 25, 45$, where the phase variable ϕ is chosen with the initial value $\bar{\phi}_0 = 0.4$, and the time step $\delta t = 1e{-}3$.

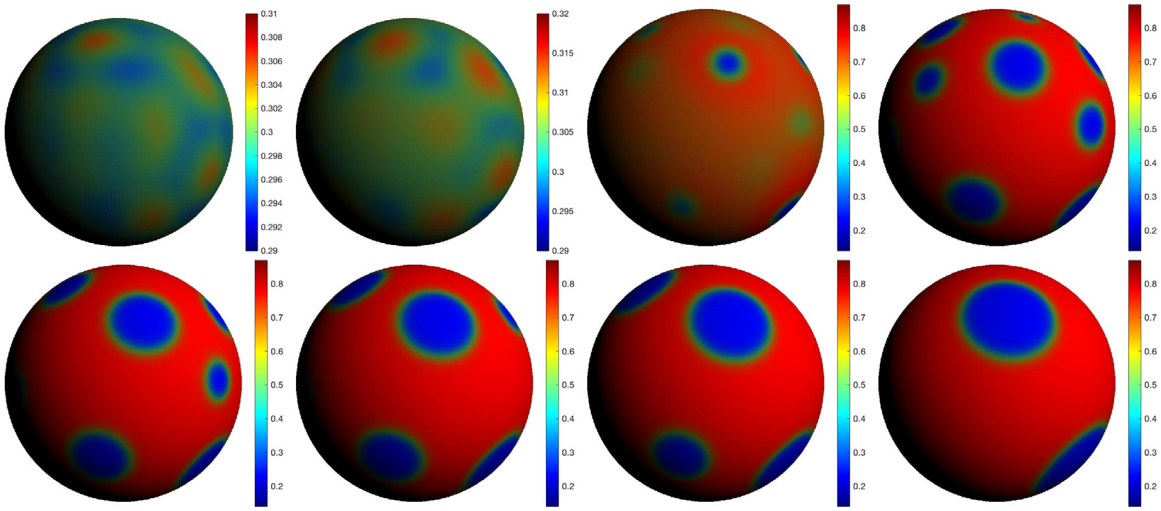

Fig. 5.5. Snapshots of the spinodal decomposition on the sphere (5.5) are taken at $t = 3, 7, 10, 15, 20, 25, 30, 50$, where the phase variable ϕ is chosen with the initial value $\bar{\phi}_0 = 0.3$, and the time step $\delta t = 1e{-}3$.

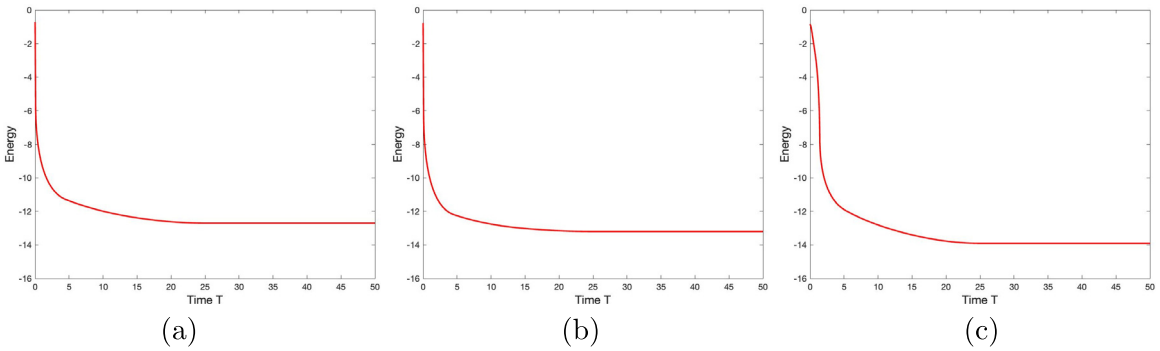

Fig. 5.6. Free energy curves on the sphere with unit radius defined as (5.5) under different initial values. (a) is $\bar{\phi}_0 = 0.5$, (b) is $\bar{\phi}_0 = 0.4$ and (c) is $\bar{\phi}_0 = 0.3$.

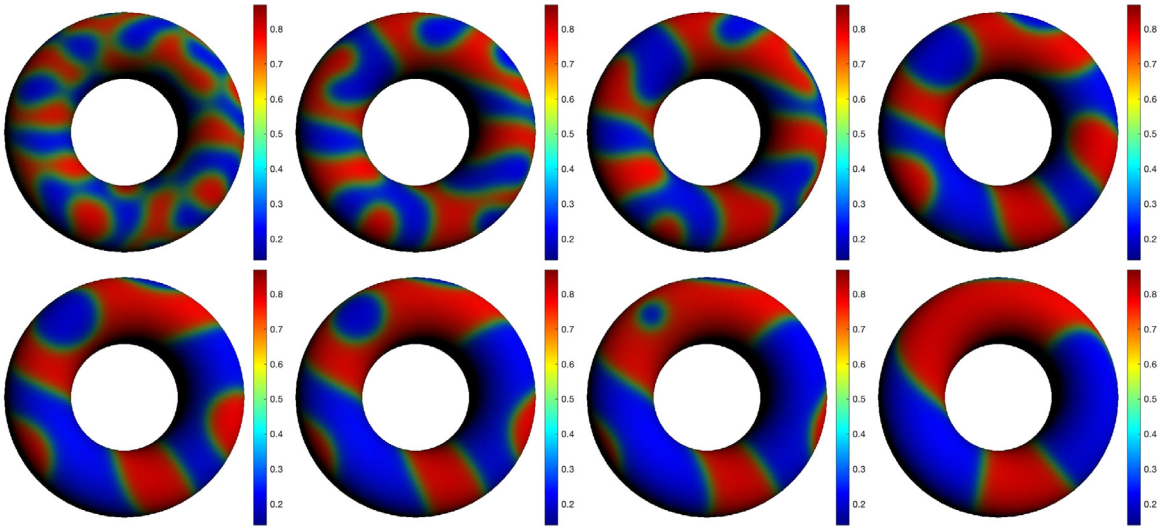

Fig. 5.7. Snapshots of the spinodal decomposition on the torus (5.7) are taken at $t = 3, 5, 10, 20, 30, 40, 50, 80$, where the phase variable ϕ is chosen with the initial value $\bar{\phi}_0 = 0.5$, and the time step $\delta t = 6\text{e}{-4}$.

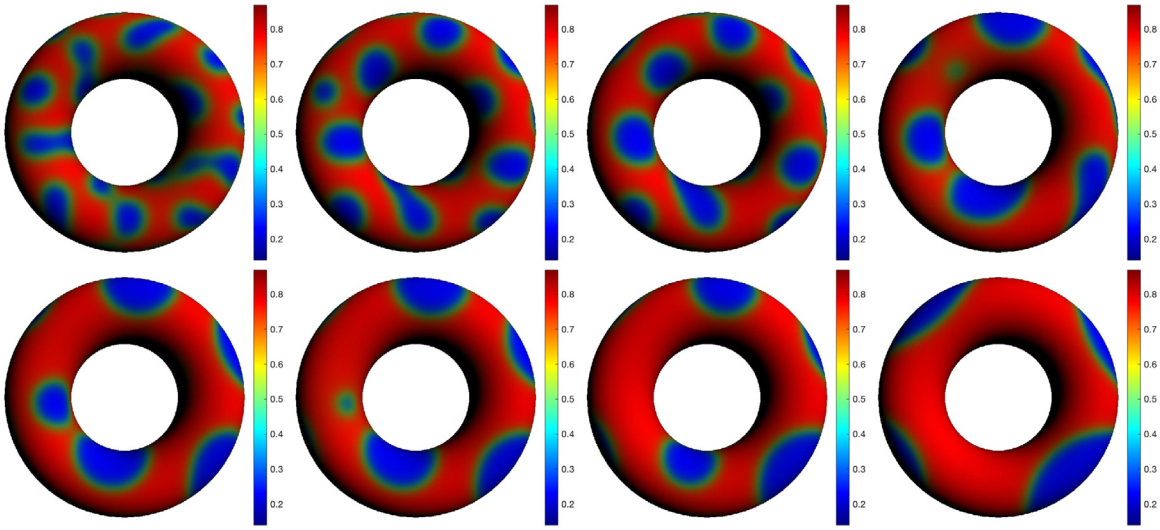

Fig. 5.8. Snapshots of the spinodal decomposition on the torus (5.7) are taken at $t = 3, 5, 10, 20, 30, 45, 60, 100$, where the phase variable ϕ is chosen with the initial value $\bar{\phi}_0 = 0.4$, and the time step $\delta t = 6\text{e}{-4}$.

which is discretized with 131072 Loop limit subdivision patches by use of 65538 control vertices, and the span of the vertex valence is 4 to 6. The parameters are given as follows:

$$\begin{aligned} M &= 1,\ \beta = 2.5,\ \varepsilon = 1\text{e}{-2},\ \sigma = 1\text{e}{-4}, \\ C &= 4\text{e}{-1},\ \eta = 4,\ B = 9\text{e}3. \end{aligned} \tag{5.6}$$

We choose three different time step sizes $\delta t = 2\text{e}{-3},\ 1\text{e}{-3}$ and $5\text{e}{-4}$ to perform the simulation until $t = 5$ with the initial condition $\bar{\phi}_0 = 0.3$ in (5.4). All of the energy curves in Fig. 5.2 show the decay about all time step sizes, which confirm the coupling scheme is unconditionally stable for any time step size.

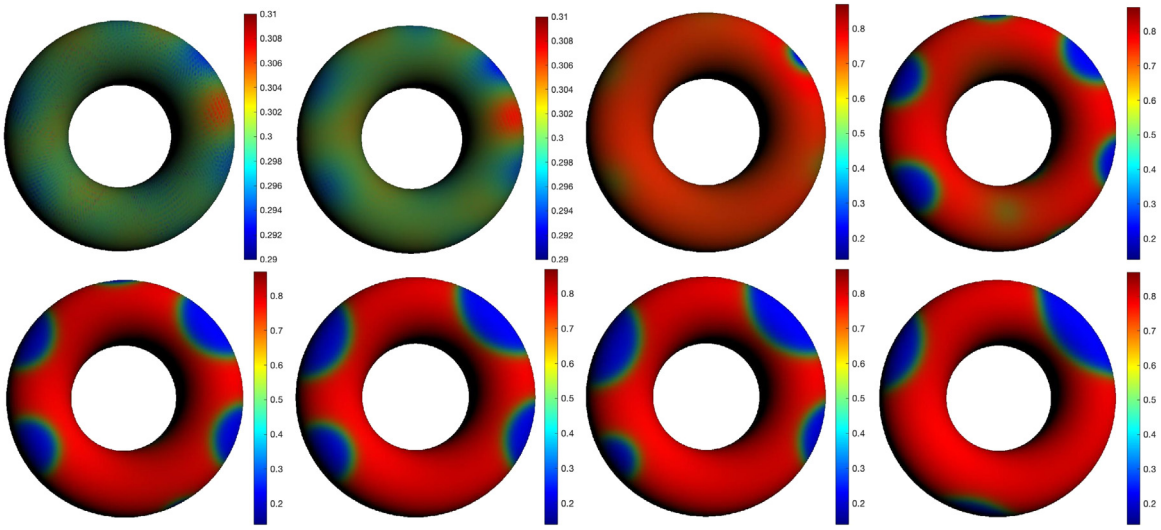

Fig. 5.9. Snapshots of the spinodal decomposition on the torus (5.7) are taken at $t = 7, 14, 20, 30, 40, 50, 70, 120$, where the phase variable ϕ is chosen with the initial value $\bar{\phi}_0 = 0.3$, and the time step $\delta t = 6e{-}4$.

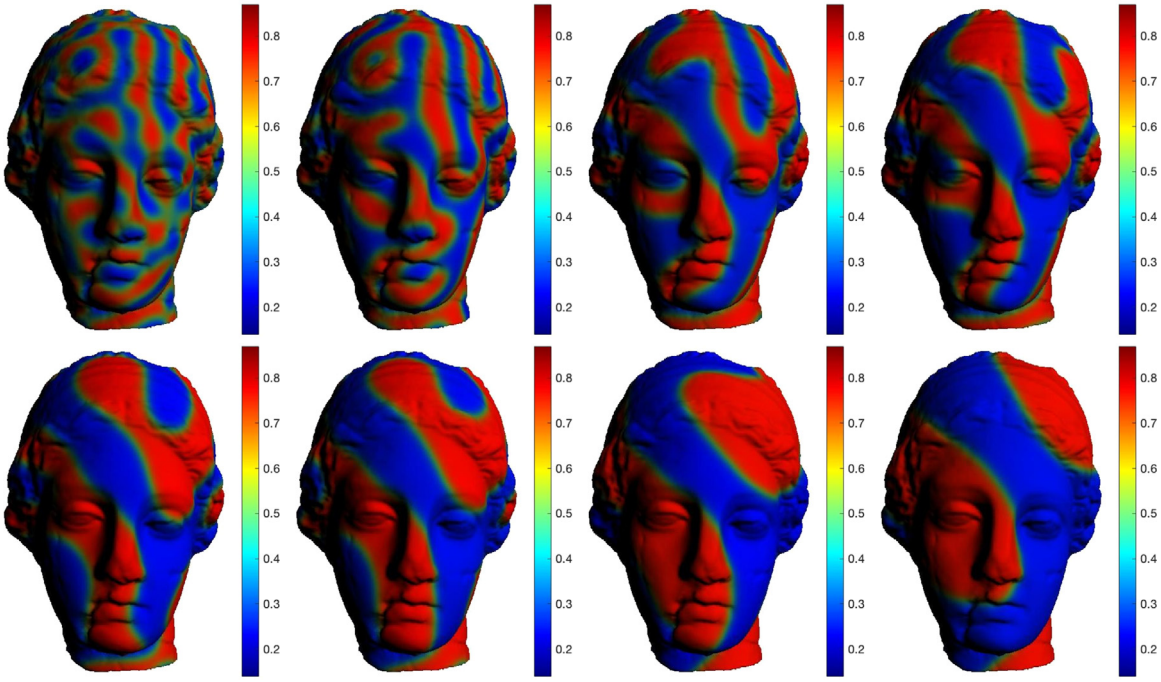

Fig. 5.10. Snapshots of the spinodal decomposition on the head (5.9) are taken at $t = 2, 6, 8, 20, 40, 60, 100, 120$, where the phase variable ϕ is chosen with the initial value $\bar{\phi}_0 = 0.5$, and the time step size $\delta t = 4e{-}4$.

Considering the surface model (5.5), we use $\delta t = 1e{-}3$ as the time step size to perform the simulations with the values of the initial condition $\bar{\phi}_0 = 0.5$, $\bar{\phi}_0 = 0.4$ and $\bar{\phi}_0 = 0.3$ respectively, and the parameters are also chosen as (5.6). We show the snapshots of the coarsening dynamics with $\bar{\phi}_0 = 0.5$ in Fig. 5.3, where the concentrated polymer segments mean the larger values of ϕ represented by red, and the macromolecular microspheres (MMs) mean the smaller values of ϕ represented by blue. When the initial value $\bar{\phi}_0 = 0.5$ meaning that both the polymer segment and the MMs have the same volume fraction, we can observe the phenomenon of partial entanglement and isolation of the chain. After the time $t = 60$, a final equilibrium solution was obtained in which the polymer segments formed bands. When the initial value $\bar{\phi}_0$ is changed to 0.4 that means the volume fraction of the MMs is larger than the polymer segment in Fig. 5.4. The polymer chains cannot be intertwined because they are too short, then they are grafted on the surface of MMS. The final steady-state solution shows that the polymer segments are clustered in some circular shapes located in the domain. When the volume fraction $\bar{\phi}_0 = 0.3$ in Fig. 5.5, its dynamical behaviors are very similar to the case of $\bar{\phi}_0 = 0.4$. The evolution curves of the free energy functional for the three initial values $\bar{\phi}_0 = 0.5$, $\bar{\phi}_0 = 0.4$ and $\bar{\phi}_0 = 0.3$ are shown in Fig. 5.6 respectively. The energy curves show the energy decays with the time that confirm our algorithm is unconditionally stable.

We perform the second simulation for a torus surface model within the domain

$$\mathcal{S}_2 = \{(x, y, z) : x \in [-4.98, 4.98],\ y \in [-4.98, 4.98],\ z \in [-1.29, 1.29]\}, \tag{5.7}$$

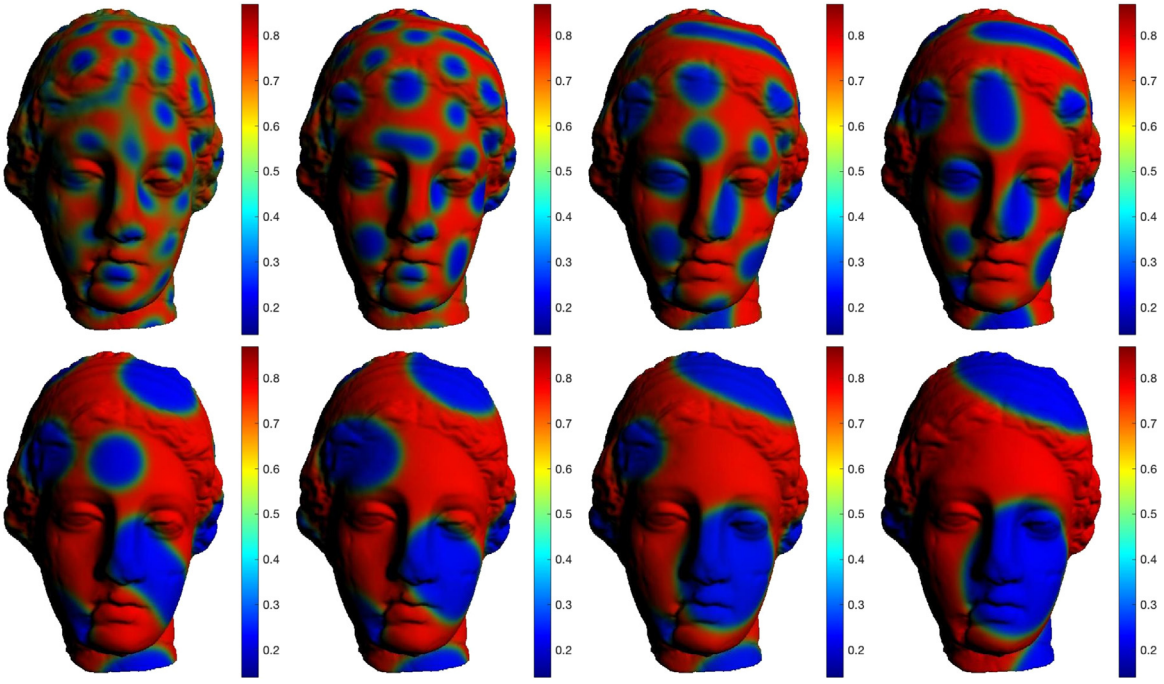

Fig. 5.11. Snapshots of the spinodal decomposition on the head (5.9) are taken at $t = 2, 6, 10, 20, 60, 80, 110, 140$, where the phase variable ϕ is chosen with the initial value $\bar{\phi}_0 = 0.4$, and the time step size $\delta t = 4\text{e}{-4}$.

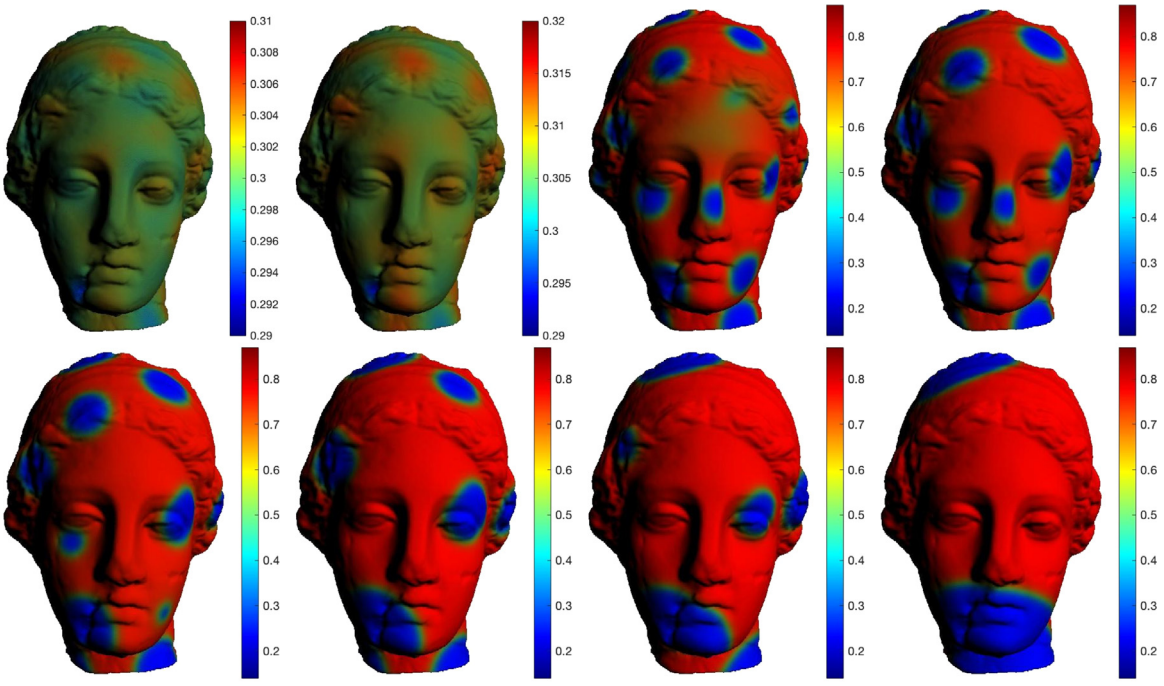

Fig. 5.12. Snapshots of the spinodal decomposition on the head (5.9) are taken at $t = 7, 14, 20, 40, 60, 80, 100, 160$, where the phase variable ϕ is chosen with the initial value $\bar{\phi}_0 = 0.3$, and the time step size $\delta t = 4\text{e}{-4}$.

which is discretized with 51200 Loop limit subdivision patches by use of 25600 control vertices, and the span of the vertex valence is [4, 8]. We choose the time step size $\delta t = 6\text{e}{-4}$, and the parameters are set as

$$\begin{aligned} &M = 1,\ \beta = 2.5,\ \varepsilon = 6\text{e}{-2},\ \sigma = 1\text{e}{-4},\\ &C = 4.5\text{e}{-1},\ \eta = 4,\ B = 9\text{e}3. \end{aligned} \tag{5.8}$$

Snapshots of the profile for the phase-field variable ϕ under the three values of the initial conditions $\bar{\phi}_0 = 0.5$, $\bar{\phi}_0 = 0.4$ and $\bar{\phi}_0 = 0.3$ are shown in Fig. 5.7, Fig. 5.8 and Fig. 5.9 respectively.

We perform the third simulation for a complex head surface model within the domain

$$\begin{aligned} \mathcal{S}_3 = \{(x, y, z) : x \in [-3.46, 3.46],\ y \in [-4.97, 4.97],\\ z \in [-4.96, 4.96]\}, \end{aligned} \tag{5.9}$$

which is discretized with 268686 Loop limit subdivision patches by use of 134345 control vertices, and the span of the vertex valence is [4, 12]. We choose the time step size $\delta t = 4\text{e}{-4}$ and

the parameters are set as

$$M = 1,\ \beta = 2.5,\ \varepsilon = 2e{-}2,\ \sigma = 1e{-}4,$$
$$C = 5.6e{-}1,\ \eta = 4,\ B = 1e4. \tag{5.10}$$

Snapshots of the profile for the phase-field variable ϕ under the three values of the initial conditions $\bar{\phi}_0 = 0.5$, $\bar{\phi}_0 = 0.4$ and $\bar{\phi}_0 = 0.3$ are shown in Fig. 5.10, Fig. 5.11 and Fig. 5.12 respectively.

6. Conclusions

In this work, we construct an IGA and EIEQ coupling scheme to numerically solve the phase-field model of homopolymer blends on complicated surfaces with arbitrary topology. The geometry of models is described with the subdivision surface approach, which has the superior capability of the refineability of B-spline techniques and the flexibility of arbitrary topology. We exploit the hierarchical structure of the subdivision-based IGA algorithm to represent the geometry of surfaces and simulate the dynamical mechanics of the particular highly nonlinear phase-field homopolymer model on the complex surface. We further present the EIEQ method in time discretization. The novel stability technique possesses high efficiency by transforming the original nonlinear system into a simple system of some elliptic equations with constant coefficients which are easy to be solved. In theory, we prove the unconditional energy stability of the second-order scheme based on the EIEQ method. Finally, by simulating several examples, we show the energy stability and the accuracy of this coupled numerical scheme. This framework of the EIEQ method coupled with the subdivision-based IGA method provides us to challenge the practical dynamical simulations on a broad range of the phase-field models on the surface.

Declaration of competing interest

The authors declare that they have no known competing financial interests or personal relationships that could have appeared to influence the work reported in this paper.

Data availability

No data was used for the research described in the article.

Acknowledgments

The work of Qing Pan was partially supported by National Natural Science Foundation of China with grant number 12171147. The work of Chong Chen was partially funded by the National Natural Science Foundation of China with grant number 12226008 and National Key Research & Development Program of China No. 2022YFC2504300 and 2022YFC2504302. The work of Jin Zhang was partially supported by Hunan Provincial Natural Science Foundation of China with grant number 2021JJ30456. The work of X. Yang was partially supported by National Science Foundation of USA with grant numbers DMS-2012490 and DMS-2309731.

References

[1] Rayleigh L. On the theory of surface forces. II Compressible fluids. Phil Mag 1892;33:209–20.
[2] van der Waals J. The thermodynamic theory of capillarity under the hypothesis of a continuous density variation. J Stat Phys 1893;20:197–244.
[3] Cahn JW, Hilliard JE. Free energy of a nonuniform system. I. Interfacial free energy. J Chem Phys 2005;28:258–67.
[4] Binder K. Collective diffusion, nucleation, and spinodal decomposition in polymer mixtures. J Chem Phys 1983;79:6387.
[5] Cahn JW, Hilliard JE. Free energy of a nonuniform system. I. Interfacial free energy. J Chem Phys 1958;28:258–67.
[6] de Gennes PG. Dynamics of fluctuations and spinodal decomposition in polymer blends. J Chem Phys 1980;7:4756.
[7] Cook HE. Brownian motion in spinodal decomposition, mouvement brownien dans la decomposition spinodale. Brownsche bewegung bei der spindodalen entmischung. Acta Metall 1970;18:297.
[8] Helf E, Sapse AM. Theory of unsymmetric polymer-polymer interfaces. J Chem Phys 1975;62:1327.
[9] McMaster LP. Aspects of liquid-liquid phase transition phenomena in multicomponent polymeric systems. copolymers, polyblends, and composites. 1975, p. 43–65.
[10] Zhai D, Zhang H. Investigation on the application of the TDGL equation in macromolecular microsphere composite hydrogel. Soft Matter 2013;9:820–5.
[11] Furihata D. A stable and conservative finite difference scheme for the Cahn–Hilliard equation. Numer Math 2001;87:675–99.
[12] Lee HG, Lowengrub JS, Goodman J. Modeling pinchoff and reconnection in a Hele-Shaw cell. II. Analysis and simulation in the nonlinear regime. Phys Fluids 2002;14:514–45.
[13] Liu C, Shen J. A phase-field model for the mixture of two incompressible fluids and its approximation by a Fourier-spectral method. Physica D 2003;179:211–28.
[14] Dziuk G, Elliot CM. Finite element methods for surface PDEs. Acta Numer 2013;22:289–396.
[15] Zhao S, Xiao X, Feng X. An efficient time adaptively based on chemical potential for surface Cahn–Hilliard equation using finite element approximation. Appl Math Comput 2020;369:124901.
[16] Du Q, Ju L, Tian L. Finite element approximation for the Cahn–Hilliard equation on surface. Comput Methods Appl Mech Engrg 2011;200:2458–70.
[17] Marenduzzo D, Orlandini E. Phase separation dynamics on curved surfaces. Soft Matter 2013;9:1178–87.
[18] Hughes TJR, Cottrell JA, Bazilevs Y. Isogeometric analysis: CAD, finite elements, NURBS, exact geometry, and mesh refinement. Comput Methods Appl Mech Engrg 2005;194:4135–95.
[19] Bazilevs Y, Beirão da Veiga L, Cottrell JA, Hughes TJR, Sangalli G. Isogeometric analysis: approximation, stability and error estimates for h-refined meshes. Math Models Methods Appl Sci 2006;16(7):1031–90.
[20] Piegl LA, Tiller W. The NURBS book (monographs in visual communication). 2nd ed. New york: Spinger-Verlag; 1997.
[21] Sederberg TW, Finnigan GT, Li X, Lin H, Ipson H. Watertight trimmed, NURBS. ACM Trans Graph 2008;27(3):1–8.
[22] Zhang Y, Bazilevs Y, Goswami S, Bajaj C, Hughes TJR. Patient-Specific vascular NURBS modeling for isogeometric analysis of blood flow. Comput Methods Appl Mech Engrg 2007;196(29–30):2943–59.
[23] Sederberg TW, Zheng J, Bakenov A, Nasri A. T-splines and T-NURCCs. ACM Trans Graph 2003;22(3):477–84.
[24] Bazilevs Y, Calo VM, Cottrell JA, Evans JA, Hughes TJR, Lipton S, et al. Isogeometric analysis using T-splines. Comput Methods Appl Mech Engrg 2010;5–8:229–63.
[25] Xie J, Xu J, Dong Z, Xu G, Deng C, Mourrain B, et al. Interpolatory Catmull–Clark volumetric subdivision over unstructured hexahedral meshes for modeling and simulation applications. Comput Aided Geom Design 2020;80:101867.
[26] Wang D, Xu J, Gao F, Wang CCL, Gu R, Lin F, et al. IGA-Reuse-NET: A deep-learning-based isogeometric analysis-reuse approach with topology-consistent parameterization. Comput Aided Geom Design 2022;95:102087.
[27] Xu G, Li B, Shu L, Chen L, Xu J, Khajah T. Efficient r-adaptive isogeometric analysis with Winslow's mapping and monitor function approach. J Comput Appl Math 2019;351:186–97.
[28] Xu G, Li M, Mourrain B, Rabczuk T, Xu J, Bordas SPA. Constructing IGA-suitable planar parameterization from complex CAD boundary by domain partition and global/local optimization. Comput Methods Appl Mech Engrg 2018;328:175–200.
[29] Xu G, Kwok TH, Wang CCL. Isogeometric computation reuse method for complex objects with topology-consistent volumetric parameterization. Comput Aided Des 2017;91:1–13.
[30] Nguyen KD, Thanh CL, Nguyen-Xuan H, Abdel-Wahab M. A hybrid phase-field isogeometric analysis to crack propagation in porous functionally graded structures. Eng Comput 2021;37(4):3017–65.
[31] Catmull E, Clark J. Recursively generated B-spline surfaces on arbitrary topological meshes. Comput Aided Des 1978;10(6):350–5.
[32] Loop C. Smooth subdivision surfaces based on triangles [Master's thesis], Department of Mathematics, University of Utah; 1978.
[33] Stam J. Fast evaluation of Catmull–Clark subdivision surfaces at arbitrary parameter values. In: SIGGRAPH '98 proceedings. 1998, p. 395–404.

[34] Pan Q, Xu G, Xu G, Zhang Y. Isogeometric analysis based on extended Loop's subdivision. J Comput Phys 2015;299(15):731–46.
[35] Pan Q, Chen C, Xu G. Isogeometric finite element approximation of minimal surfaces based on extended Loop subdivision. J Comput Phys 2017;343:324–39.
[36] Pan Q, Rabczuk T, Xu G, Chen C. Isogeometric analysis for surface PDEs with extended Loop subdivision. J Comput Phys 2019;398:108892.
[37] Pan Q, Rabczuk T, Chen C. Subdivision based isogeometric analysis for geometric flows. Internat J Numer Methods Engrg 2022;123:610–33.
[38] Pan Q, Xu G, Xu G, Zhang Y. Isogeometric analysis based on extended Catmull–Clark subdivision. Comput Math Appl 2016;71:105–19.
[39] Pan Q, Rabczuk T, Xu G, Chen C. Isogeometric analysis of minimal surfaces on the basis of extended Catmull–Clark subdivisions. Comput Methods Appl Mech Engrg 2018;337:128–49.
[40] Pan Q, Rabczuk T, Yang X. Subdivision-based isogeometric analysis for second order partial differential equations on surfaces. Comput Mech 2021;68:1205–21.
[41] Wei X, Zhang Y, Hughes TJR, Scott MA. Truncated hierarchical Catmull–Clark subdivision with local refinement. Comput Methods Appl Mech Engrg 2015;291:1–20.
[42] Wei X, Li X, Zhang YJ, Hughes TJR. Tuned hybrid Non-Uniform subdivision surfaces with optimal convergence rates. Internat J Numer Methods Engrg 2021;122(9):2117–44.
[43] Cirak F, Ortiz M, Schröder P. Subdivision surfaces: a new paradigm for thin-shell finite-element analysis. Int J Numer Methods Eng 2000;47:2039–72.
[44] Cirak F, Scott MJ, Antonsson EK, Ortiz M, Schröder P. Integrated modeling, finite-element analysis, and engineering design for thin-shell structures using subdivision. Comput Aided Des 2002;34(2):137–48.
[45] Eyre DJ. Unconditionally gradient stable time marching the Cahn–Hilliard equation. In: Computational and mathematical models of microstructural evolution. San Francisco, CA, 1998. Mater. res. soc. symp. proc, vol. 529, Warrendale, PA: MRS; 1998, p. 39–46.
[46] Chen R, Ji G, Yang X, Zhang H. Decoupled energy stable schemes for phase-field vesicle membrane model. J Comput Phys 2015;302:509–23.
[47] Shen J, Yang X. Numerical approximations of Allen-Cahn and Cahn–Hilliard equations. Discrete Contin Dyn Syst Ser A 2010;28:1169–691.
[48] Xu C, Tang T. Stability analysis of large time-stepping methods for epitaxial growth models. Liq Cryst 2006;44:1759–79.
[49] Yang X. Linear, first and second-order, unconditionally energy stable numerical schemes for the phase-field model of homopolymer blends. J Comput Phys 2016;327:294–316.
[50] Yang X, Yu H. Efficient Second order unconditionally stable schemes for a phase-field moving contact line model using an Invariant Energy Quadratization approach. SIAM J Sci Comput 2018;40:889–914.
[51] Yang X, Zhao J, Wang Q, Shen J. Numerical for a three components Cahn–Hilliard phase-field Model based on the Invariant Energy Quadratization method. Math Models Methods Appl Sci 2017;27(11):1993–2030.
[52] Zhao J, Yang X, Gong Y, Wang Q. A Novel linear second order unconditionally energy stable scheme for a hydrodynamic Q-Tensor model of liquid crystals. Comput Methods Appl Mech Engrg 2017;318:803–25.
[53] Pan Q, Chen C, Zhang Y, Yang X. A novel hybrid IGA-EIEQ numerical method for the Allen–Cahn/Cahn–Hilliard equations on complex curved surfaces. Comput Methods Appl Mech Engrg 2023;404:115767.
[54] Yang X. On a novel full decoupling, linear, second-order accurate, and unconditionally energy stable numerical scheme for the anisotropic phase-field dendritic crystal growth model. Internat J Numer Methods Engrg 2021;122:4129–53.
[55] Bray AJ. An introduction to the kinetics of first-order phase transitions. Adv Phys 1994;43:357.
[56] Copetti MIM, Elliott CM. Numerical analysis of the Cahn–Hilliard equation with a logarithmic free energy. Numer Math 1992;63(4):39–65.
[57] Stam J. Fast evaluation of loop triangular subdivision surfaces at arbitrary parameter values. In: SIGGRAPH '98, CD-ROM supplement. 1998.
[58] Zhu J, Chen L, Shen J, Tikare V, Zhu J, Chen L, et al. Coarsening kinetics from a variable-mobility Cahn–Hilliard equation: application of a semi-implicit Fourier spectral method. Phys Rev E 1999;60(4):3564–72.
[59] Fialkowski M, Holys R. Dynamics of phase separation in polymer blends revisited: morphology, spinodal, noise, and nucleation. Macromol Theory Simul 2008;17:263.
[60] Li X, Ji G, Zhang H. Phase transitions of macromolecular microsphere composite hydrogels based on the stochastic Cahn–Hilliard equation. J Comput Phys 2015;283:81–97.
[61] Yuan C, Zhang H. Self-consistent mean field model of hydrogel and its numerical simulation. J Theor Comput Chem 2013;12:1350048.